RSC Advances

PAPER

View Article Online
View Journal | View Issue

Cite this: *RSC Adv.*, 2017, **7**, 17020

Hydrothermally prepared nanosized and mesoporous $Ce_{0.4}Zr_{0.6}O_2$ solid solutions with shape dependence in photocatalysis for the degradation of methylene blue†

Wei Tian,[a] Jun Yin,[b] Lingfei Wei,[a] Quanhao Shen,[a] Rehana Bibi,[a] Ming Liu,[a] Bin Yang,[a] Naixu Li*[a] and Jiancheng Zhou*[acd]

Received 27th January 2017
Accepted 6th March 2017

DOI: 10.1039/c7ra01201b

rsc.li/rsc-advances

Mesoporous $Ce_{0.4}Zr_{0.6}O_2$ solid solutions with four different shapes, including mixed nanorod and nanoparticle (RP, cubic), nanopolyhedron (PH, tetragonal), nanosphere (SP, cubic) and nanoegg (EG, tetragonal), were hydrothermally fabricated. Various physical and chemical techniques were used to reveal shape-dependent structural, optical, electronic and surface properties, providing a powerful insight into the morphological dependence of photocatalytic activity towards methylene blue (MB) degradation. Among these samples, RP, consisting of a cubic Ce-rich phase ($Ce_{0.6}Zr_{0.4}O_2$ nanorods) and a tetragonal Zr-rich phase ($Ce_{0.2}Zr_{0.8}O_2$ nanoparticles), affords the optimal functionality, with a top degradation rate (D = 70.5%) and a peak rate constant (k = 0.0102 min^{-1}). This occurrence results mainly from the prompt separation of excitons and suitable textural properties for MB absorption and activation. A brief introduction to the reaction path when using RP is proposed.

Introduction

Semiconductor-based photocatalytic technology is highly appreciated as a promising and powerful response to human concerns over the energy crisis and environmental contamination, by virtue of the use of inexhaustible and renewable solar radiation as a substitute for non-renewable resources, such as coal and petroleum.[1–4] This appealing feature considerably prompts its versatile application in H_2 evolution,[5–9] CO_2 utilization[10–12] and environmental cleaning.[13–17] It is unquestionable that the exploration of photocatalytic materials of high activity and stability is an indispensable part of its development. Over the past few years, the focusing of great attention on the advanced structural, optical and electronic properties of semiconductors has remarkably inspired the design and fabrication of exciting light-responsive materials based on TiO_2 (ref. 18–20) and titanates,[14,21,22] metal sulfides,[23–27] g-C_3N_4 (ref. 28–31) and WO_3 (ref. 13 and 32) from abundantly available feedstocks, leading to an incredible expansion in their application to areas involving photocatalysis and photothermalcatalysis.

Apart from the aforementioned catalytic materials, there are other first-rank analogues of substantial interest. In particular, CeO_2, a well-documented typical pale yellow/white rare earth oxide with non-stoichiometric properties and a face-centered cubic (f.c.c.) fluorite structure, is endowed with special characteristics including but not limited to (a) outstanding (photo) chemical and thermal stability, low toxicity and cost,[33] (b) redox, acid–base bifunctional and semiconducting features that are hardly accessible in other materials[34,35] and (c) facile fabrication using various existing protocols from earth-abundant starting materials.[36–38] However, the material hardly escapes its intrinsic defects, such as weak surface acid strength and the low separation efficiency of charge barriers, which are detrimental for practical applications. Great efforts connected with countering these issues, mainly including structural and chemical modifications, have accelerated a collection of amazing catalytic breakthroughs in a broad array of diverse applications ranging from the oxidation of pollutants to H_2 evolution and fuel cells to photo(thermal)catalysis.[34,39]

The structurally functionalized design of CeO_2 is mainly classified into two groups: the construction of a specific morphology (*e.g.* nanorod, nanocube, nanopolyhedron or nanotube)[40] and the introduction of porous behavior (*e.g.* mesoporous or macroporous) through template-assisted methods[41,42]. The morphology dependence of (photo)catalytic performance is more widely

[a]*School of Chemistry and Chemical Engineering, Southeast University, Nanjing 211189, Jiangsu, PR China. E-mail: naixuli@seu.edu.cn; jczhou@seu.edu.cn*

[b]*Department of Biological and Chemical Engineering, Jingdezhen College, Jingdezhen 333000, Jiangxi, PR China*

[c]*Department of Chemical and Pharmaceutical Engineering, Southeast University Chengxian College, Nanjing 210088, Jiangsu, PR China*

[d]*Jiangsu Province Hi-Tech Key Laboratory for Bio-medical Research, Southeast University, Nanjing 211189, PR China*

† Electronic supplementary information (ESI) available: Experimental and characterization details and some related results from characterization and photocatalytic performance evaluation. See DOI: 10.1039/c7ra01201b

observed and well-rationalized using tunable active atomic modes on preferentially exposed reactive planes through the precise control of thermodynamics and kinetics in material preparation.[43–45] For example, Wang *et al.*[46] developed CeO_2 nanorods, nanocubes, octahedrons and spindles through careful command of the hydrothermal process, including hydrothermal temperature and time, and the category and concentration of mineralizers for dimethyl carbonate (DMC) synthesis from CO_2 and methanol. The author confirmed shape-dependent exposed facets with designated acid and basic strength through TEM, SEM and TPD results. On the other hand, spindle-like CeO_2 enclosed by a (111) crystal plane turn out to be most catalytically active among the four shapes possibly associated with the exposed (111) plane, defect sites, and acidic-basic sites. Notably, from a kinetic viewpoint, weak acid sites played a major role in the elevated catalysis due to the appropriate strength available for reactant adsorption and resultant desorption, as compared to moderate and strong sites. In other words, in this system, CeO_2 acted as acid–base bifunctional promoter, which offered shape-controlled catalytic performance. Lu *et al.*[47] correlated shapes with photocatalysis (redox behavior) by using hexagonal CeO_2 nanorods as a catalyst for photocatalytic hydrogen evolution. Rod-shaped CeO_2 provided an elevated hydrogen evolution rate (HER) relative to CeO_2 nanoparticles. The occurrence was closely associated with Ce^{3+} and oxygen vacancies. CeO_2 rods enclosed by exposed less stable {110} planes accommodated more Ce^{3+} and oxygen vacancies than CeO_2 nanoparticles with the most stable {111} facets predominantly exposed. These two factors respectively encouraged a boost in light absorption and the separation efficiency of excitons,[34,48] resulting in a remarkable increase in the HER. To conclude, morphology has an evident effect on photocatalysis.

Chemically modified CeO_2, through doping with foreign elements or the constructing a CeO_2-based hybrid system, has been a research hotspot both in academia and the industrial community. Chemical doping proves an effective strategy to tailor the physical and chemical properties of catalytic materials to improve their performances.[49–51] The first transition series metals, Zr and rare earth elements are preferentially selected for CeO_2 modification. Liyanage *et al.*[48] made a detailed comparison of the catalytic performance towards the photothermalcatalytic degradation of indigo carmine and rhodamine B over hydrothermally prepared Y doped CeO_2 rods (Ce–Y–O solid solutions, YOC). Compared with the pristine analogue, YOC displayed higher photocatalytic activity below 50% Y doping. Among doped samples, YOC with 10% loading was above others when ranked in terms of catalysis. The observation was intimated to be related to the bandgap (optical harvesting capacity) and oxygen vacancies (separation efficiency of excitons, as set forth) as a function of Y concentration. Thus, the optimal light-driven catalytic activity was obtained through setting a reasonable Y concentration (10% loading). The conclusion is also applied to CeO_2 doping with other metals, such as Mn,[52,53] Zr[54] and Sn.[55] Among these elements, Zr draws extensive attention among scholars. Zhang *et al.*[54] prepared tetragonal $Ce_xZr_{1-x}O_2$ ($x = 0.1$, 0.2 and 0.3) solid solutions *via* a citrate complexation route and evaluated their catalytic function in the photocatalytic decolourization of rhodamine B (RhB) and 2,4-dichorophenol (2,4-DCP). They proved more catalytically active than pure CeO_2, partly due to the former amplified visible-light response resulting from the visible-light-induced metal-to-metal charge transfer (MMCT) transition ("Zr(IV)–O–Ce(III)" → "Zr(III)–O–Ce(IV)") in a specific oxo-bridged bimetallic Zr(IV)–O–Ce(III) linkage between two neighboring flattened tetrahedrons of the structural framework. This occurrence distinguishes them from their analogues, including Y doped CeO_2 nanorods[48] and $Zn_xCd_{1-x}S$,[23,25] ignoring a conventional concept that the optical absorption of a solid solution is supposed to fall in between those of its parent compounds.

In addition to chemical doping, coupling plain or doped CeO_2 with some useful materials to construct a series of CeO_2-based functionalized assemblies has enjoyed tremendous publicity in the past few decades. Among these, plain or doped CeO_2 (dominated by CeO_2 and $Ce_xZr_{1-x}O_2$) serves as an active support for noble metals (*e.g.* Pt[56,57] and Au[58,59]) and metal oxides (*e.g.* NiO_x (ref. 60 and 61)) or essential components of supporting materials.[62,63] Although they show striking advances in thermal catalysis, they fail to receive due attention in photo(thermal)catalysis.

As can be seen from the aforementioned introduction, CeO_2 of various shapes and $Ce_xZr_{1-x}O_2$ solid solutions have been well explored, but investigating the morphological effects of $Ce_xZr_{1-x}O_2$ solid solutions on photocatalytic activity remains an untouched area to date. Herein, we hydrothermally access nanosized $Ce_{0.4}Zr_{0.6}O_2$ with four different shapes, RP, PH, SP and EG. To begin with, a comparative study on the photocatalytic removal of methylene blue (MB) over $Ce_xZr_{1-x}O_2$ ($0 \leq x \leq 1$) obtained using the synthetic strategy for RP indicates $Ce_{0.4}Zr_{0.6}O_2$ RP as the optimal catalyst (Table S1†). Therefore, $x = 0.4$ was fixed in following experiments. Next, as-prepared samples were characterized using XRD, Raman, EDS-mapping, SEM, TEM, XPS, DRS, photocurrent response, N_2 sorption, and NH_3- and CO_2-TPD. Different acid–base behaviors from TPD analyses not only correspond to various separation efficiencies for photogenerated charges, but also state the preferentially exposed reactive facets of samples with various shapes. Furthermore, photocatalytic activity tests confirm $Ce_{0.4}Zr_{0.6}O_2$ RP as the best of the four catalysts, which derives mainly from the prompt separation of excitons and suitable textural properties that favor MB adsorption and activation. Finally, based on analytical results, a possible reaction mechanism was proposed.

Results and discussion

XRD and Raman analysis

Structural characteristics of various samples are revealed unambiguously through XRD and Raman studies in Fig. S1† and Fig. 1. Fig. S1a† indicates that CeO_2 and ZrO_2 samples respectively crystallize in face-centered cubic fluorite and tetragonal structures, from consulting their individual PDF cards (PDF#34-0394 and PDF#50-1089). Besides, a successive shift in all patterns to higher diffraction angles with increasing Zr content is clearly observed, indicative of $Ce_xZr_{1-x}O_2$ as

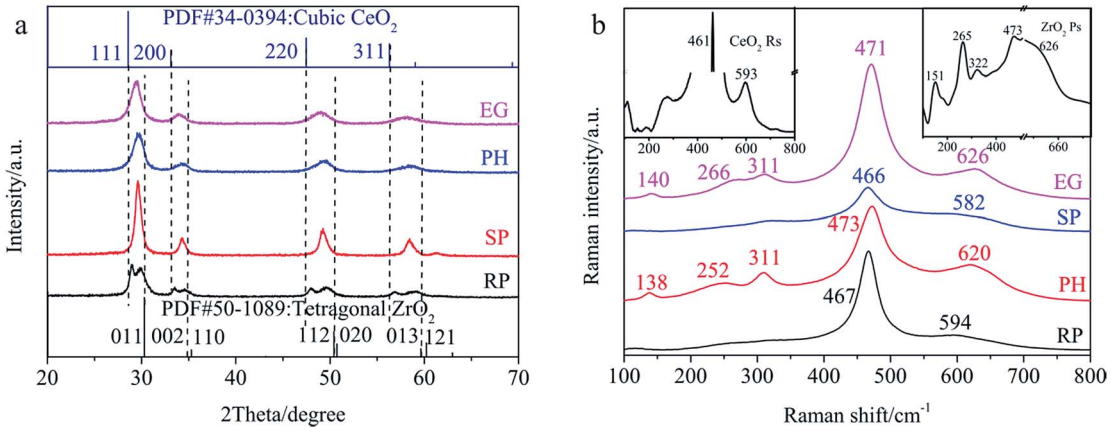

Fig. 1 (a) XRD patterns and (b) Raman spectra of $Ce_{0.4}Zr_{0.6}O_2$ solid solutions with different shapes ("Raman shift/cm^{-1}" and "Raman intensity/a.u." are applied to the longitudinal and horizontal coordinates of the insets, the Raman spectra of CeO_2R and ZrO_2 P).

a typical solid solution.[54] The idea is also highly approved upon seeing that the evidently depressed peak intensities of each CeO_2–ZrO_2 sample compared with pristine oxides discloses the introduction of Ce^{4+} (Zr^{4+}) into the ZrO_2 (CeO_2) framework, which is similar to previous results[15,16]. Interestingly, unlike homogeneous $Ce_xZr_{1-x}O_2$ ($x = 0.2$, 0.6 and 0.8), $Ce_{0.4}Zr_{0.6}O_2$ RP is identified as a diphasic solid due to peak splitting. In addition, by virtue of cubic CeO_2 and tetragonal ZrO_2, as well as biphasic $Ce_{0.4}Zr_{0.6}O_2$, $Ce_xZr_{1-x}O_2$ samples are reasonably assumed to be cubic ($x \geq 0.4$) and tetragonal ($x < 0.4$) systems. Therefore, an RP-shaped sample is composed of a CeO_2-rich phase (cubic $Ce_{0.6}Zr_{0.4}O_2$) and a ZrO_2-rich phase (tetragonal $Ce_{0.2}Zr_{0.8}O_2$) from a comparative analysis of their XRD patterns.[34] The results are made clearer in the locally magnified Fig. S1a† (Fig.S1b†).

Fig. 1a provides solid evidence that PH, SP and EG-shaped $Ce_{0.4}Zr_{0.6}O_2$ are characterized as uniphase solid solutions by virtue of (a) the respective appearance of peaks around 29.8°, 34.8°, 49.6° and 58.3° between (111), (200), (220) and (311) in cubic CeO_2 and (011), (002), (112) and (013) in tetragonal ZrO_2 (marked with dashed lines) and (b) the absence of a combined XRD pattern for pure CeO_2 and ZrO_2, excluding the formation of CeO_2–ZrO_2 composites.[50] However, it is very difficult to make accurate judgments regarding the crystalline phase of each solid solution using XRD alone. The issue has been well addressed with the aid of Raman analysis.[54] Fig. 1b presents Raman spectra of samples with four shapes, along with those of pristine CeO_2 R and ZrO_2 P as reference samples, provided as insets. Obviously, in the left inset, a steep peak centered at 461 cm^{-1}, ascribed to the Raman active F_{2g} vibration mode of the cubic phase, suggests pure CeO_2 with a cubic syngony,[48,54,64] which is consistent with the XRD results. In addition, the other peak at *ca.* 593 cm^{-1} in the inset reveals a small amount of Ce^{3+} cations in the CeO_2 network.[48] The two observations equally happen in RP and SP-shaped materials, implying their cubic-fluorite structures with a small amount of Ce^{3+} ions, similar to pure CeO_2. However, with respect to the two other samples, the bands around 140, 266, 311, 471 and 626 cm^{-1} stem from Raman active models ($A_{1g} + 2B_{1g} + 3E_g$) of tetragonal ZrO_2 (the right inset), denoting their tetragonal nature.[54] Combining XRD and Raman results, lattice spacings (d) and relevant planes are certainly determined and summarized in Table S2.†

Electron microscopy analysis

Fig. S2–S5† provide STEM images and corresponding mappings of $Ce_{0.4}Zr_{0.6}O_2$ with various morphologies defining well the element components and distributions. To begin with, Fig. S2e† recognizes markedly $Ce_{0.4}Zr_{0.6}O_2$ RP, which can be divided into two parts: Group R and Group P (Fig. S2d and f†). Each group is composed of three homogeneously distributed elements: Ce, Zr and O (Fig. S2a–c and g–i†). Notably, Group R embraces a Ce-rich and Zr-lean phase ($Ce_{0.59}Zr_{0.41}O_2$, from the EDS results, as below), which is opposite to that of Group P ($Ce_{0.21}Zr_{0.79}O_2$). To conclude, when integrated with XRD and Raman analyses, cubic $Ce_{0.4}Zr_{0.6}O_2$ RP is well-defined as a solid solution assembly of cubic $Ce_{0.6}Zr_{0.4}O_2$ R and tetragonal $Ce_{0.2}Zr_{0.8}O_2$ P. Judging from the evenly dispersed Ce, Zr and O in Fig. S3–S5,† three other samples are equally identified as $Ce_{0.4}Zr_{0.6}O_2$ solid solutions, which is in line with the respective XRD results. Nevertheless, these shaped bodies are too small to discern only *via* STEM micrographs. Thus, SEM and HRTEM are of exceptional importance for this purpose.

Fig. 2 allows the analysis of the morphology and grain size of each $Ce_{0.4}Zr_{0.6}O_2$ material. As seen from Fig. 2a, $Ce_{0.4}Zr_{0.6}O_2$ embodies rod-like bodies, with lengths of up to *ca.* 400–500 nm and a peak diameter of up to *ca.*100 nm, and morphologically irregular particulate matter on a nanometer scale. In Fig. 2b, an irregular shaped particle with a tetragonal structure is intimately attached to the R-shaped matrix. In addition, RP displays four sets of lattice fringes with interplanar crystal spacing of 0.293, 0.293, 0.254 and 0.18 nm, respectively corresponding to the (111), (011), (200) and (220) planes. Finally, the lattice spacing of 0.543 nm is indexed as the lattice constant (a) of the $Ce_{0.6}Zr_{0.4}O_2$ solid solution.[65]

With the exception of RP, another three samples are difficult to identify in shape from their SEM graphs (Fig. 2c, e and g) due to relatively smaller particles (*ca.*10–45 nm in size). HRTEM

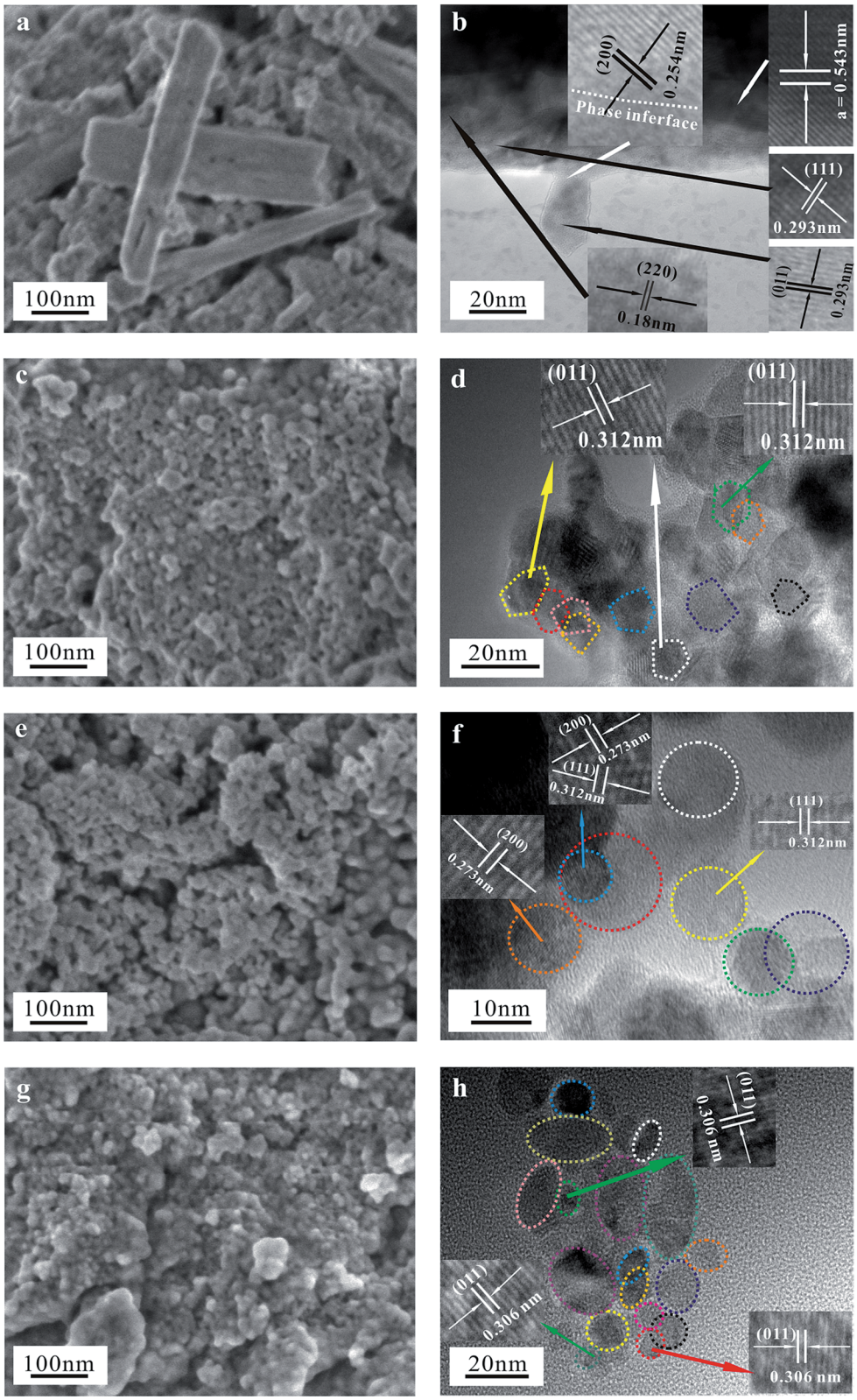

Fig. 2 SEM and HRTEM images of $Ce_{0.4}Zr_{0.6}O_2$ RP (a and b), PH (c and d), SP (e and f) and EG (g and h).

images completely differentiate their nanoscale morphologies. In Fig. 2d, tetragonal $Ce_{0.4}Zr_{0.6}O_2$ PH, with clear-cut edges and corners (highlighted with various coloured polygons), shows a narrow edge length distribution of 4–15 nm and a (011) facet with lattice spacing of 0.312 nm. As shown in Fig. 2f, the cubic SP-like solid solution is well constructed with a diameter range

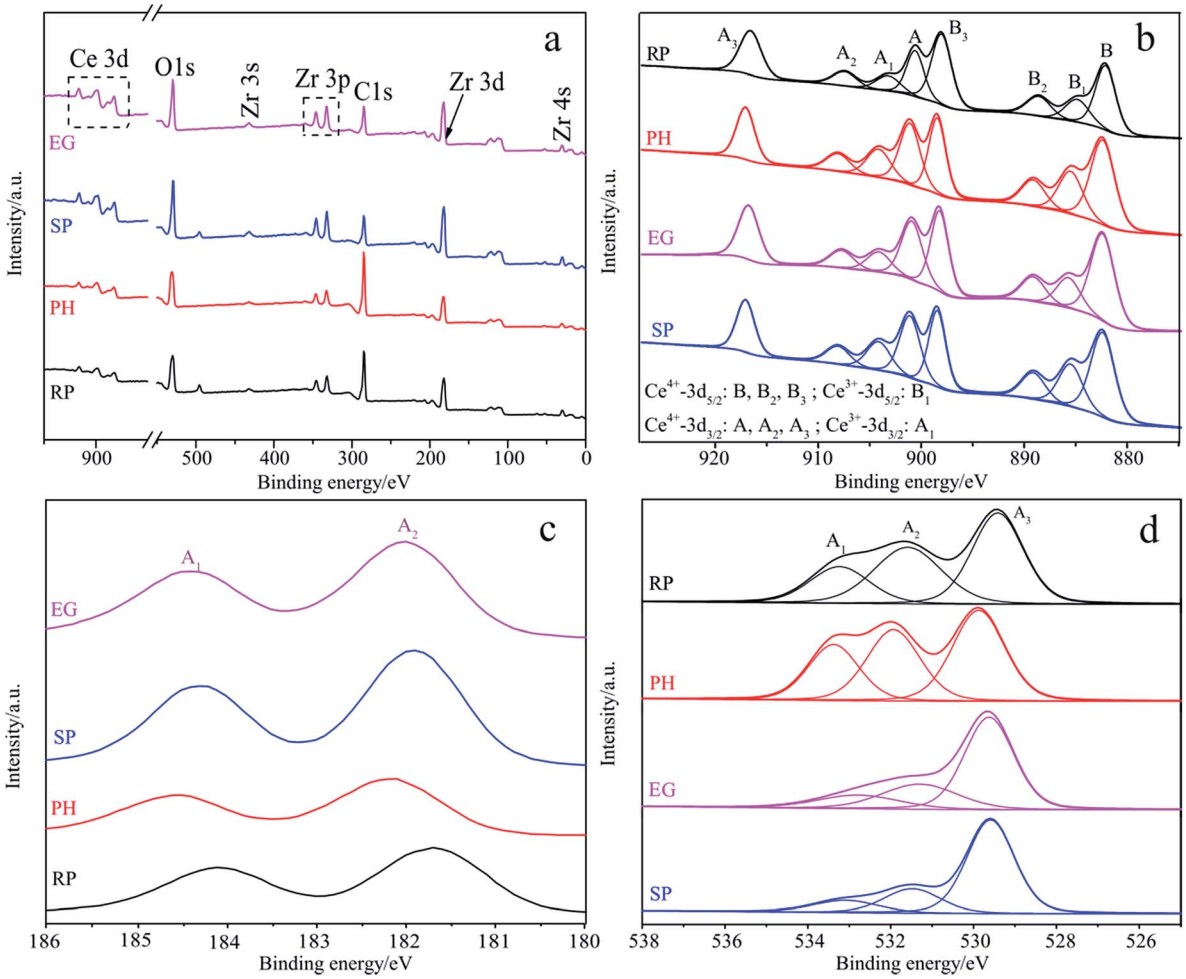

Fig. 3 Survey spectra (a) and high-resolution XPS spectra of Ce 3d (b), Zr 3d (c) and O 1s (d) for four samples with various shapes.

of 8–16 nm, and is enclosed by (111) and (200) planes with interplanar distances of 0.312 and 0.273 nm, respectively. Fig. 2h unequivocally elucidates an interesting tetragonal EG-shaped sample of (5 × 7)–(17 × 33) nm^2, long × short axis, with a lattice spacing of 0.306 nm, ascribed to (011) facets. In all cases, the perfect agreement of the lattice spacings from HRTEM with corresponding data from XRD analysis (Table S2,† no. 4, 7–9) again substantiates the formation of solid solutions.

XPS analysis

To fully investigate surface components and the chemical state of samples, XPS spectra are provided in Fig. 3, along with related important data on binding energies (Table S3†) and on the content of designated species (Table S4†) for four different shaped samples. The survey spectra in Fig. 3a offer solid evidence of Ce, Zr and O as the basic elements of all shape-dependent samples, which is in good agreement with the mapping results. In addition, the real components of these samples (Table S4†) are calculated from the corresponding peak areas provided by CasaXPS software. Obviously, these XPS data are roughly consistent with those obtained using EDS, with the exception of RP. However, both display some deviation from the theoretical values, possibly due to the irregular surfaces of the determinant or other technical limitations in both. Fig. 3b depicts the intricate Ce 3d spectrum associated with a tunable valence state and a particular 4f configuration.[66] It is well-decomposed into Series A (900.6–917.0 eV) and B (882.3–898.5 eV), which are assigned to the spin–orbit coupling Ce $3d_{3/2}$ and Ce $3d_{5/2}$ states, respectively.[65] Among the two, A_1 and B_1 are indexed as Ce^{3+}, and others as Ce^{4+}.[66] The binding energies of 882.3–882.6 eV in Series B being below that of bulk CeO_2 (882.9 eV) support the evaluation of all samples as solid solutions[67] as the XRD and mapping results also do. Besides, Ce^{3+} content is obtained from a peak area percentage of A_1 and B_1 in Series A and Series B. As seen from Table S4,† it follows the rank: PH > SP > EG ≈ RP, which coincides with that for oxygen defect concentration, which is directly proportional to the former. In Fig. 3c, the characteristic doublets positioned at *ca.* 182 and *ca.* 184 eV respectively, related to core-level Zr $3d_{5/2}$ and $3d_{3/2}$, support Zr^{n+} ($4 > n > 0$) and Zr^{4+} species, the former providing second convincing evidence for well-constructed solid solutions with adjustable shapes.[54,67] Fig. 3d elaborates the deconvolution of the high resolution O 1s profile into three peaks centered at 529.4–533.4 eV, which are respectively ascribed to Ce–O, Zr–O and H–O bonds.[66,67] Each O species content is sensitive to

sample shape, especially for those in the same crystal system (*e.g.* for A_1s of RP and SP, a marked margin of up to 8.5%, Table S4†). O species content is expected to impact the surface acid–base nature (Table 1) in close relation with the separation efficiency of light-induced excitons.

DRS, VBXPS and *I–V* analyses

UV-Vis diffuse reflection spectroscopy (DRS), valence band XPS (VBXPS) and photocurrent–voltage (*I–V*) curves are collected in Fig. 4 for a comparison of the optical absorption capacity, the construction of the energy band structure and the evaluation of separation probability of light-driven excitons. Fig. 4a displays typical semiconducting and shape-dependent optical absorption with a sole and steep absorption band in the ultraviolet and visible window of the solar spectrum for each sample. RP, SP, PH and EG shaped materials display absorption bands near 431, 458, 480 and 497 nm, respectively. Cubic SP is higher in rank, possibly due to enhanced Ce^{3+} content relative to that of cubic RP[48] (Table S4†). With regard to tetragonal CeO_2–ZrO_2, such as EG and PH-shaped bodies (Fig. 1b), a robust visible-light response benefits partially from a metal-to-metal charge transfer (MMCT) transition in the oxo-bridged Zr(IV)–O–Ce(III) linkage.[54] The former is slightly more light-responsive than the latter, primarily on account of having more access to the transition. A comparative analysis of light harvesting between the two phases deals with the two effects above. In the case of EG and SP-like bodies, the MMCT transition plays the main part in the former optical excellence. In the advantageous optical absorption see in PH over that of SP, both may work together.

The inset in Fig. 4a offers bandgap (E_g) values (2.87–3.14 eV) from a Tauc plot interpretation based on the following equation:[13,21,68]

$$\alpha h\nu = A(h\nu - E_g)^{n/2} \quad (1)$$

where α, n, E_g and A represent the absorption coefficient, the light frequency, the band gap and a constant, respectively. In all cases, $n = 1$. VB positions ($E_{VB} = 2.56$–3.16 eV) of these samples with various shapes determined using VBXPS are exhibited in Fig. 4b. Their conduction band potentials (E_{CB}) are calculated using the expression below:[13,15,16]

$$E_{CB} = E_{VB} - E_g \quad (2)$$

Therefore, their E_{CB} values are determined to be −0.58 (RP), 0.25 (PH), −0.32 (SP) and 0.29 eV (EG), respectively.

Comparative resolution of the separation efficiencies of light-induced charge carriers is conducted by means of an *I–V* curve under Xe lamp irradiation (Fig. 4c). The four differently shaped bodies exhibit significant differences in net photocurrent response as an indicator of separation efficiency. These efficiencies follow the order: RP ≈ SP > EG > PH, which is inconsistent with the optical responses (Fig. 4a) but accords well with that of the surface acid–base amounts (Table 1). In a word, the optical properties, band structures and excitonic separations of a semiconductor are largely dependent on its morphology.

N_2 sorption analysis

N_2 sorption profiles in Fig. 5 are used to shed light on the textural properties of specific morphological samples. All sorption curves in Fig. 5a display an adsorption jump in the P/P_0 range of *ca.* 0.4–1.0. They are classified into (a) typical type-II isotherm curves with a clear H3-type hysteresis loop, which applies to the cubic RP and SP-shaped samples[21,69] and (b) type-IV isothermal absorption models of a typical mesoporous material with a H2 hysteresis loop, suitable for tetragonal $Ce_{0.4}Zr_{0.6}O_2$ PHs and EGs.[70] Fig. 5b describes shape-related BJH pore width distributions centered at 9.51, 11.5, 13.6 and 3.61 nm for RP, PH, SP and EG-shaped materials, indicating their mesoporous structures.

It is well documented that the textural properties of a catalytic material have a remarkable effect on the adsorption and activation of reagents such as methylene blue (MB) on its surface. Table S5† collects important data comprising of BET surface areas (S_{BET}), pore volumes (PV), average pore sizes (APS) and methylene blue absorbances (MBA) associated with this behaviour. Obviously, the SP-shaped body with enhanced textural properties ($S_{BET} = 63.0$ m^2 g^{-1} and PV = 0.237 cm^3 g^{-1}) relative to those of the RP analogue ($S_{BET} = 39.6$ m^2 g^{-1} and PV = 0.150 cm^3 g^{-1}) provides elevated MBA (41.1% *vs.* 29.6%). Nevertheless, the substitution of PH ($S_{BET} = 47.0$ m^2 g^{-1} and PV = 0.164 cm^3 g^{-1}) with identical superiority for SP in the aforementioned discussion enables a completely opposite result (1.56% *vs.* 29.6%). The two occurrences are rationalized by the N_2 sorption profiles (Fig. 5). With respect to samples such as SP and RP with identical types of isotherm curves and hysteresis loops, their textural properties feature as the basis for

Table 1 Acidic and basic amounts in $Ce_{0.4}Zr_{0.6}O_2$ samples with tunable shapes from CO_2-TPD and NH_3-TPD

	NH_3 absorption (mmol g^{-1})[a]				CO_2 absorption (mmol g^{-1})[b]			
Samples	Weak (<200 °C)	Moderate (200–400 °C)	Strong (>600 °C)	Total	Weak (<200 °C)	Moderate (200–400 °C)	Strong (>600 °C)	Total
RP	0.184	0.349	0.148	0.681	0.155	0.324	Trace	0.479
PH	0.245	0.258	nd[c]	0.503	0.184	0.149	nd	0.333
SP	0.320	0.452	nd	0.772	0.288	0.317	nd	0.605
EG	0.281	0.379	nd	0.660	0.257	0.257	nd	0.514

[a] NH_3-TPD results. [b] CO_2-TPD results. [c] nd = not detected.

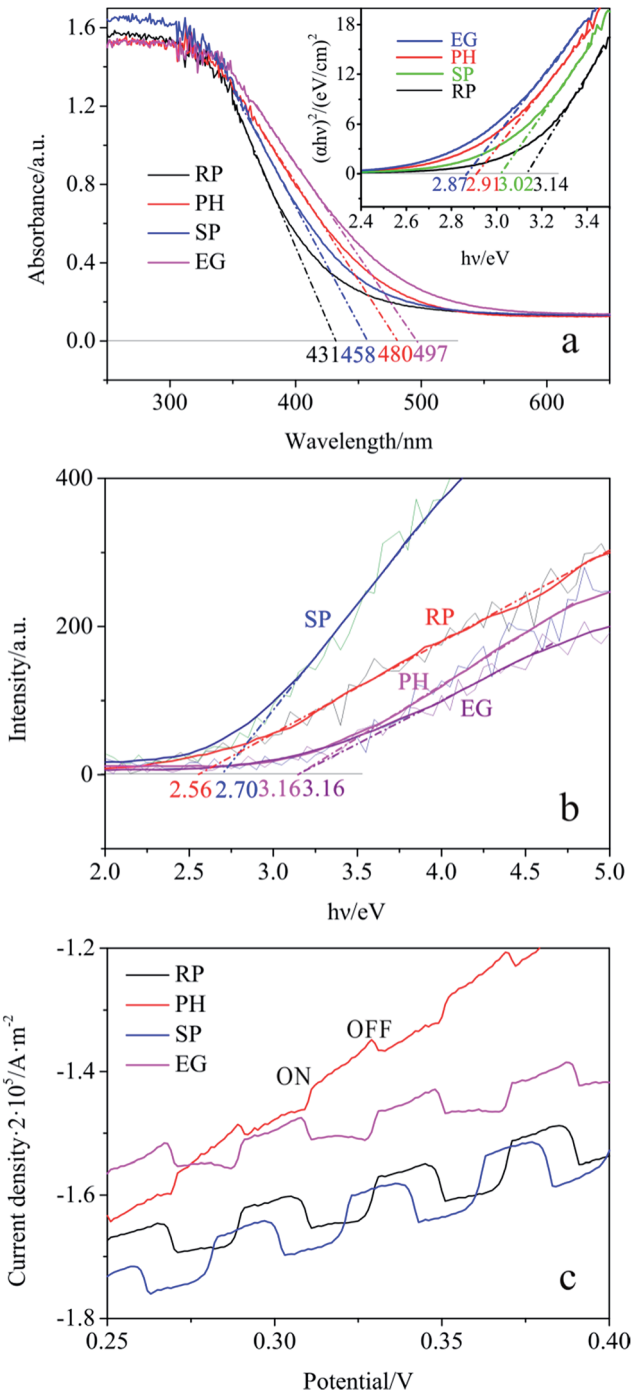

Fig. 4 DRS and Tauc plots (inset) (a), VBXPS profiles (b) and *I*–*V* curves (c) of samples with different shapes.

an estimation of their adsorption capacity for a given adsorbate. So do those of EG and PH (a small pore size in the tetragonal phase represents superiority from the viewpoint of MB adsorption). If not, the relationship is hardly well established and thus analysed experimentally. Such is the case for EG and RP. As indicated from Table S5,† tetragonal materials prove inefficient in MB absorption and activation, which is hazardous for its removal.

NH_3-and CO_2-TPD analysis

Enhanced surface acid–base characteristics of samples are reported to allow the suppressed recombination of light-induced excitons, leading to improved photocatalytic performance.[71–73] Therefore, this is well-examined by means of NH_3- and CO_2-TPD techniques. Fig. S7† and Table 1 summarize three types of acid–base sites and their amounts in the four shaped samples, respectively. Fig. S7† indicates the classification of these sites into weak (<200 °C), moderate (200–400 °C) and strong (>600 °C) ones. PH, EG and SP-like bodies merely cover the first two. Both numbers follow the order: SP > EG > PH (Table 1), which is in good agreement with the separation efficiencies of charge carriers (Fig. 4c), implying that increased acidity and alkalinity favour excitonic splitting. Unlike the three other materials, the RP-shaped sample embraces all three sites possibly associated with its phase separation. Notably, its exclusive strong acidic sites endow it with as good separation effects for electron–hole pairs as that of an SP-like analogue (Fig. 4c). In addition, the marked variation in the amounts of acid–base sites represents different anion–cation layouts on the exposed surfaces of variously shaped bodies. That is to say, the samples with various shapes tune their surface acid–base properties for the control of excitonic separation efficiencies by selectively exposing reactive facets to obtain desirable photocatalytic performances.

Photocatalytic performance evaluation

MB photocatalytic removal serves as a target reaction to test the catalytic functionality of four samples with different shapes. Fig. 6 illustrates the rank of their activities: RP > EG > SP > PH (Fig. 6a), along with the fact that the reaction is a first-order kinetic process (Fig. 6b). A comprehensive analysis of the aforementioned characterization conclusions, especially those from Fig. 4 and 5 and Table 1, sheds light on the sequence. Of the four, the RP-like solid is selected as the undisputed champion by virtue of its advantages, including (a) the desirable separation probability of the photogenerated charges (Fig. 4c) resulting from the optimal acid–base behavior (Fig. S7† and Table 1) by selectively exposing the designated reactive planes, and (b) the suitable textural properties for efficient MB adsorption and activation (Fig. 5 and Table S5†), over those of the three other samples in the dominant factors that influence photocatalytic behavior. Next, compared with the RP-like solid, the elevated light harvesting capacity (Fig. 4a) of the EG-like material among the four is not sufficient to rectify the undesirable situation caused by the aforementioned factors. In addition, SP loses its predomination, that equals or surpasses the first two, in that it suffers from excessively large S_{BET} and PV values (Table S5†) and imperfect optical behavior (Fig. 4a), despite its superior separation efficiency. The former is adverse to the resultant desorption and light input of the reaction system by virtue of exorbitantly adsorbed MB. The latter enables the obstruction of photogenerated electron–hole pairs. Finally, the most catalytically inactive PH-shaped body suffers mainly from exceptionally low MB absorbance (Table S5†), hardly absorbing and activating MB, and unsatisfactory splitting attributes toward excitons (Fig. 4c).

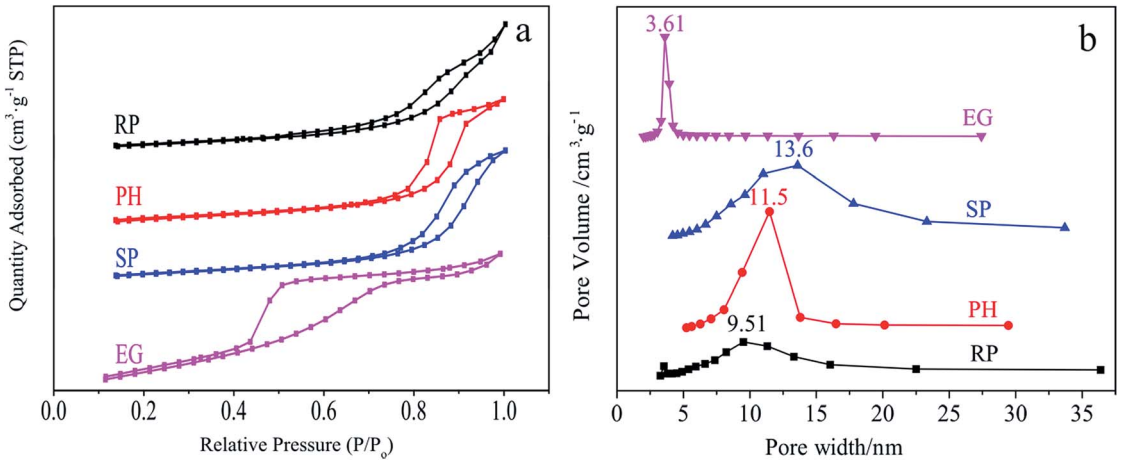

Fig. 5 N_2 sorption (a) and BJH pore size distribution (b) of RP, PH, SP and EG-shaped samples.

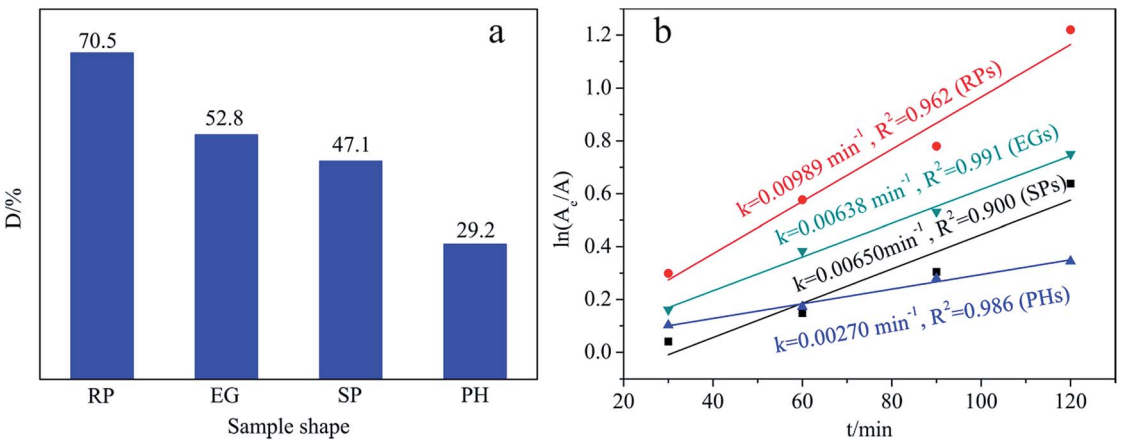

Fig. 6 (a) Degradation efficiency (*D*) and (b) reaction rate constant (*k*) of samples with different shapes.

Conclusions

RP, PH, SP and EG-like $Ce_{0.4}Zr_{0.6}O_2$ materials were synthesized *via* a technically viable hydrothermal route. These materials are endowed with unique physical and chemical behaviors as a function of shape that are well-determined by means of various tools including XRD, Raman, EDS-mapping, SEM, TEM, XPS, N_2 sorption, NH_3- and CO_2-TPD, DRS and photocurrent response. Therefore, the morphological dependence of light-induced catalytic performance is well-established. Among the aforementioned samples, RP stands out from its photocatalytically active competition with the three other samples by means of its excellence in excitonic splitting and textural properties. A possible reaction mechanism is proposed based on the well-identified main reactive species.

Acknowledgements

This work was financially supported by the Fundamental Research Funds for the Central Universities of China (No. 3207045403 and 3207045409), the National Natural Science Foundation of China (No. 21576050 and No. 51602052), the Jiangsu Provincial Natural Science Foundation of China (BK20150604) and a Project Funded by the Priority Academic Program Development of Jiangsu Higher Education Institutions (PAPD).

Notes and references

1 Y. J. Zhang, T. Mori and J. H. Ye, *Sci. Adv. Mater.*, 2012, **4**, 282–291.
2 Y. Ma, X. L. Wang, Y. S. Jia, X. B. Chen, H. X. Han and C. Li, *Chem. Rev.*, 2014, **114**, 9987–10043.
3 H. Xu, S. X. Ouyang, L. Q. Liu, P. Reunchan, N. Umezawa and J. H. Ye, *J. Mater. Chem. A*, 2014, **2**, 12642–12661.
4 H. J. Li, Y. Zhou, W. G. Tu, J. H. Ye and Z. G. Zou, *Adv. Funct. Mater.*, 2015, **25**, 998–1013.
5 M. C. Liu, L. Z. Wang, G. Q. Lu, X. D. Yao and L. J. Guo, *Energy Environ. Sci.*, 2011, **4**, 1372–1378.
6 M. Liu, Y. Chen, J. Su, J. Shi, X. Wang and L. Guo, *Nat. Energy*, 2016, **1**, 16151.

7 N. X. Li, M. C. Liu, Z. H. Zhou, J. C. Zhou, Y. M. Sun and L. J. Guo, *Nanoscale*, 2014, **6**, 9695–9702.
8 N. X. Li, L. Z. Zhang, J. C. Zhou, D. W. Jing and Y. M. Sun, *Dalton Trans.*, 2014, **43**, 11533–11541.
9 Q. W. Tian, L. Zhang, J. H. Liu, N. X. Li, Q. H. Ma, J. C. Zhou and Y. M. Sun, *RSC Adv.*, 2015, **5**, 734–739.
10 X. Meng, T. Wang, L. Liu, S. Ouyang, P. Li, H. Hu, T. Kako, H. Iwai, A. Tanaka and J. Ye, *Angew. Chem., Int. Ed.*, 2014, **53**, 11478–11482.
11 T. Wang, X. G. Meng, P. Li, S. X. Ouyang, K. Chang, G. G. Liu, Z. W. Mei and J. H. Ye, *Nano Energy*, 2014, **9**, 50–60.
12 X. Meng, S. Ouyang, T. Kako, P. Li, Q. Yu, T. Wang and J. Ye, *Chem. Commun.*, 2014, **50**, 11517–11519.
13 N. Li, H. Teng, L. Zhang, J. Zhou and M. Liu, *RSC Adv.*, 2015, **5**, 95394–95400.
14 J. H. Liu, L. Zhang, N. X. Li, Q. W. Tian, J. C. Zhou and Y. M. Sun, *J. Mater. Chem. A*, 2015, **3**, 706–712.
15 W. Tian, N. Li and J. Zhou, *Appl. Surf. Sci.*, 2016, **361**, 251–258.
16 W. Tian, Q. Shen, N. Li and J. Zhou, *RSC Adv.*, 2016, **6**, 25568–25576.
17 J. Wang, Y. Shen, Y. Li, S. Liu and Y. Zhang, *Chem.–Eur. J.*, 2016, **22**, 12449–12454.
18 Q. Kang, T. Wang, P. Li, L. Q. Liu, K. Chang, M. Li and J. H. Ye, *Angew. Chem., Int. Ed.*, 2015, **54**, 841–845.
19 H. Xu, P. Reunchan, S. Ouyang, H. Tong, N. Umezawa, T. Kako and J. Ye, *Chem. Mater.*, 2013, **25**, 405–411.
20 N. Li, M. Liu, B. Yang, W. Shu, Q. Shen, M. Liu and J. Zhou, *J. Phys. Chem. C*, 2017, **121**, 2923–2932.
21 L. Zhang, W. Tian, Y. Chen, J. Chen, H. Teng, J. Zhou, J. Shi and Y. Sun, *RSC Adv.*, 2016, **6**, 83471–83481.
22 C. J. Xing, D. W. Jing, M. C. Liu and L. J. Guo, *Mater. Res. Bull.*, 2009, **44**, 442–445.
23 M. C. Liu, D. W. Jing, Z. H. Zhou and L. J. Guo, *Nat. Commun.*, 2013, **4**, 1–8.
24 M. Liu and X. Wang, *SPIE Newsroom*, 2016, DOI: 10.1117/2.1201604.006486.
25 N. X. Li, B. Y. Zhou, P. H. Guo, J. C. Zhou and D. W. Jing, *Int. J. Hydrogen Energy*, 2013, **38**, 11268–11277.
26 M. C. Liu, B. Wang, Y. Q. Zheng, F. Xue, Y. B. Chen and L. J. Guo, *Catal. Sci. Technol.*, 2016, **6**, 3371–3377.
27 M. C. Liu, D. W. Jing, L. A. Zhao and L. J. Guo, *Int. J. Hydrogen Energy*, 2010, **35**, 7058–7064.
28 Z. X. Zhou, J. H. Wang, J. C. Yu, Y. F. Shen, Y. Li, A. R. Liu, S. Q. Liu and Y. J. Zhang, *J. Am. Chem. Soc.*, 2015, **137**, 2179–2182.
29 Z. Zhou, Y. Shen, Y. Li, A. Liu, S. Liu and Y. Zhang, *ACS Nano*, 2015, **9**, 12480–12487.
30 Z. Zhou, Q. Shang, Y. Shen, L. Zhang, Y. Zhang, Y. Lv, Y. Li, S. Liu and Y. Zhang, *Anal. Chem.*, 2016, **88**, 6004–6010.
31 J. Shi, C. Cheng, Y. Hu, M. Liu and L. Guo, *Int. J. Hydrogen Energy*, 2017, **42**, 4651–4659.
32 N. Li, Y. Zheng, L. Wei, H. Teng and J. Zhou, *Green Chem.*, 2017, **19**, 682–691.
33 K. Wu, L. D. Sun and C. H. Yan, *Adv. Energy Mater.*, 2016, **6**, 1600501.
34 T. Montini, M. Melchionna, M. Monai and P. Fornasiero, *Chem. Rev.*, 2016, **116**, 5987–6041.
35 L. Vivier and D. Duprez, *Chemsuschem*, 2010, **3**, 654–678.
36 Y. D. Liu, J. Goebl and Y. D. Yin, *Chem. Soc. Rev.*, 2013, **42**, 2610–2653.
37 R. I. Walton, *Prog. Cryst. Growth Charact. Mater.*, 2011, **57**, 93–108.
38 A. Varma, A. S. Mukasyan, A. S. Rogachev and K. V. Manukyan, *Chem. Rev.*, 2016, **116**, 14493–14586.
39 G. Nahar and V. Dupont, *Renewable Sustainable Energy Rev.*, 2014, **32**, 777–796.
40 C. W. Sun, H. Li and L. Q. Chen, *Energy Environ. Sci.*, 2012, **5**, 8475–8505.
41 D. Terribile, A. Trovarelli, J. Llorca, C. de Leitenburg and G. Dolcetti, *J. Catal.*, 1998, **178**, 299–308.
42 Y. Wei, Z. Zhao, J. Liu, C. Xu, G. Jiang and A. Duan, *Small*, 2013, **9**, 3957–3963.
43 Y. Li and W. J. Shen, *Chem. Soc. Rev.*, 2014, **43**, 1543–1574.
44 M. C. Liu, Y. Q. Zheng, S. F. Xie, N. X. Li, N. Lu, J. G. Wang, M. J. Kim, L. J. Guo and Y. N. Xia, *Phys. Chem. Chem. Phys.*, 2013, **15**, 11822–11829.
45 M. C. Liu, Y. Q. Zheng, L. Zhang, L. J. Guo and Y. N. Xia, *J. Am. Chem. Soc.*, 2013, **135**, 11752–11755.
46 S. P. Wang, L. F. Zhao, W. Wang, Y. J. Zhao, G. L. Zhang, X. B. Ma and J. L. Gong, *Nanoscale*, 2013, **5**, 5582–5588.
47 X. H. Lu, T. Zhai, H. N. Cui, J. Y. Shi, S. L. Xie, Y. Y. Huang, C. L. Liang and Y. X. Tong, *J. Mater. Chem.*, 2011, **21**, 5569–5572.
48 A. D. Liyanage, S. D. Perera, K. Tan, Y. Chabal and K. J. Balkus, *ACS Catal.*, 2014, **4**, 577–584.
49 Y. J. Zhang, T. Mori, J. H. Ye and M. Antonietti, *J. Am. Chem. Soc.*, 2010, **132**, 6294–6295.
50 X. H. Zhang, D. W. Jing, M. C. Liu and L. J. Guo, *Catal. Commun.*, 2008, **9**, 1720–1724.
51 Y. J. Zhang, T. Mori, L. Niu and J. H. Ye, *Energy Environ. Sci.*, 2011, **4**, 4517–4521.
52 L. Yue and X.-M. Zhang, *J. Alloys Compd.*, 2009, **475**, 702–705.
53 P. Borker and A. V. Salker, *Mater. Chem. Phys.*, 2007, **103**, 366–370.
54 C. C. Zhang and J. Lin, *Phys. Chem. Chem. Phys.*, 2011, **13**, 3896–3905.
55 H. R. Pouretedal, Z. Tofangsazi and M. H. Keshavarz, *J. Alloys Compd.*, 2012, **513**, 359–364.
56 J. C. Serrano-Ruiz, J. Luettich, A. Sepúlveda-Escribano and F. Rodríguez-Reinoso, *J. Catal.*, 2006, **241**, 45–55.
57 Q. Yuan, Q. Liu, W.-G. Song, W. Feng, W.-L. Pu, L.-D. Sun, Y.-W. Zhang and C.-H. Yan, *J. Am. Chem. Soc.*, 2007, **129**, 6698–6699.
58 A. Primo, T. Marino, A. Corma, R. Molinari and H. García, *J. Am. Chem. Soc.*, 2011, **133**, 6930–6933.
59 Q. Xu, W. Lei, X. Li, X. Qi, J. Yu, G. Liu, J. Wang and P. Zhang, *Environ. Sci. Technol.*, 2014, **48**, 9702–9708.
60 G. Nahar, V. Dupont, M. V. Twigg and E. Dvininov, *Appl. Catal., B*, 2015, **168–169**, 228–242.
61 T. Mondal, K. K. Pant and A. K. Dalai, *Int. J. Hydrogen Energy*, 2015, **40**, 2529–2544.
62 N. S. Arul, D. Mangalaraj, R. Ramachandran, A. N. Grace and J. I. Han, *J. Mater. Chem. A*, 2015, **3**, 15248–15258.
63 M. J. Muñoz-Batista, M. N. Gómez-Cerezo, A. Kubacka, D. Tudela and M. Fernández-García, *ACS Catal.*, 2014, **4**, 63–72.

64 Y. Wei, Z. Zhao, J. Liu, S. Liu, C. Xu, A. Duan and G. Jiang, *J. Catal.*, 2014, **317**, 62–74.
65 Y. Zhang, J. Wen, J. Wang, D. Pan, M. Shen and Y. Lu, *Nano Res.*, 2011, **4**, 494–504.
66 P. Ji, J. Zhang, F. Chen and M. Anpo, *J. Phys. Chem. C*, 2008, **112**, 17809–17813.
67 G. Postole, B. Chowdhury, B. Karmakar, K. Pinki, J. Banerji and A. Auroux, *J. Catal.*, 2010, **269**, 110–121.
68 S. Ouyang, P. Li, H. Xu, H. Tong, L. Liu and J. Ye, *ACS Appl. Mater. Interfaces*, 2014, **6**, 22726–22732.
69 N. Li, L. Wei, R. bibi, L. Chen, J. Liu, L. Zhang, Y. Zheng and J. Zhou, *Fuel*, 2016, **185**, 532–540.
70 S. Zeng, X. Zhang, X. Fu, L. Zhang, H. Su and H. Pan, *Appl. Catal., B*, 2013, **136–137**, 308–316.
71 X. C. Wang, J. C. Yu, Y. D. Hou and X. Z. Fu, *Adv. Mater.*, 2005, **17**, 99–102.
72 Y. H. Zhang, G. X. Xiong, N. Yao, W. S. Yang and X. Z. Fu, *Catal. Today*, 2001, **68**, 89–95.
73 Z. Z. Lin and X. C. Wang, *Angew. Chem., Int. Ed.*, 2013, **52**, 1735–1738.